Steel and Composite Structures, *Vol. 30, No. 4 (2019) 365-382*
DOI: https://doi.org/10.12989/scs.2019.30.4.365

Finite element analysis for the seismic performance of steel frame-tube structures with replaceable shear links

Ming Lian *, Hao Zhang, Qianqian Cheng and Mingzhou Su

School of Civil Engineering, Xi'an University of Architecture and Technology, Xi'an, China

(*Received August 24, 2018, Revised February 15, 2019, Accepted February 21, 2019*)

Abstract. In steel frame-tube structures (SFTSs) the application of flexural beam is not suitable for the beam with span-to-depth ratio lower than five because the plastic hinges at beam-ends can not be developed properly. This can lead to lower ductility and energy dissipation capacity of the SFTS. To address this problem, a replaceable shear link, acting as a ductile fuse at the mid length of deep beams, is proposed. SFTS with replaceable shear links (SFTS-RSLs) dissipate seismic energy through shear deformation of the link. In order to evaluate this proposal, buildings were designed to compare the seismic performance of SFTS-RSLs and SFTSs. Several sub-structures were selected from the design buildings and finite element models (FEMs) were established to study their hysteretic behavior. Static pushover and dynamic analyses were undertaken in comparing seismic performance of the FEMs for each building. The results indicated that the SFTS-RSL and SFTS had similar initial lateral stiffness. Compared with SFTS, SFTS-RSL had lower yield strength and maximum strength, but higher ductility and energy dissipation capacity. During earthquakes, SFTS-RSL had lower interstory drift, maximum base shear force and story shear force compared with the SFTS. Placing a shear link at the beam mid-span did not increase shear lag effects for the structure. The SFTS-RSL concentrates plasticity on the shear link. Other structural components remain elastic during seismic loading. It is expected that the SFTS-RSL will be a reliable dual resistant system. It offers the benefit of being able to repair the structure by replacing damaged shear links after earthquakes.

Keywords: steel frame-tube structure (SFTS); replaceable shear link; hysteretic behaviors; dynamic behaviors; finite element analyses

1. Introduction

Steel moment resisting frames (MRFs) have high ductility and energy dissipation capacity. These lateral load resisting systems are widely used in structural engineering. Steel MRFs are designed to dissipate earthquake energy by inelastic deformation of flexural hinges at beam-ends. After the 1994 Northridge and 1995 Kobe earthquakes, many studies were carried out on the beam-to-column connections and details used in steel MRFs to improve the hysteretic behaviors of flexural hinges at beam-ends. Results indicated that these new beam-to-column connections could improve seismic performance and efficiency of steel MRFs (Ramirez *et al*. 2012, Sheet *et al*. 2013, Memari *et al*. 2014, Oh *et al*. 2015, Bahrami *et al*. 2017). Moreover, in order to ensure sufficient length of flexural plastic hinges at beam-ends, it limited use of these beam-to-column connections to clear span-to-depth ratios greater than seven in special MRFs and five in intermediate MRFs in AISC 358-10 and FEMA-335D.

Steel frame-tube structures (SFTSs) are effective high-rise structural systems. They have great lateral stiffness due to closely spaced perimeter columns interconnected by deep spandrel beams that form the tube. This allows the building to behave as a huge vertical cantilever to resist overturning moments. By placing columns at 3.0 m to 4.0 m intervals, with spandrel beam depth varying from 0.6 to 1.5 m, span-to-depth ratios are usually between 2.0 and 4.4 (Taranath 2011). It has been shown that the application of flexural beam loading prevents adequate development of plastic hinges at beam-ends for span-to-depth ratios less than five. This leads to lower energy dissipation capacity and poor seismic performance of such SFTS designs. Furthermore, considering the great stiffness of deep spandrel beams and the composite action of floor slab, plastic deformation may initially occur at column-ends thus increasing the possibility of collapse. During severe earthquakes, considering occupancy performance levels, such SFTS designs may result in unacceptable losses and costs. Considering the poor seismic performance of SFTSs, most studies focus on the simplified elastic analysis method for SFTSs (Charney and Pathak 2008a, b, Moon 2010, Kamgar and Rahgozar 2013). Few mentioned seismic performance. In response to this situation, many researchers began examining the combined system of framed tube, shear core and outrigger-belt truss in high-rise building design. For this system, the effects of applying higher order axial displacement distribution to solve a continuum model were investigated (Rahgozar *et al*. 2014). A continuous-discrete approach was proposed for free vibration analysis (Malekinejad *et al*. 2016). The design method and optimal belt truss location were also investigated (Alavi *et al*. 2018, Tavakoli *et al*.

*Corresponding author, Ph.D., Associate Professor,
E-mail: lianming0821@163.com

ISSN: 1229-9367 (Print), 1598-6233 (Online)

2018).

In eccentrically braced frames (EBFs), a shear link exhibits stable hysteretic performance and energy dissipative capacity (Shayanfar *et al*. 2012, Lian *et al*. 2015, 2017, Okazaki and Engelhardt 2015, Caprili *et al*. 2018). The replaceable shear links can be used in structure as ductile fuses, which will make the damage mainly occur at replaceable shear links during severe earthquakes and the other structural components are still in elastic, so that the structures can be repaired and continue to resist the seismic loads just using the new shear links replace the damage ones. This has obvious benefits for structural integrity and repair costs. Replaceable shear links can be used as ductile fuses at the mid length of deep beams with low span-to-depth ratios. In steel frame-tube structures with replaceable shear links (SFTS-RSLs), the replaceable shear link has a smaller shear capacity than that of the beam, so that the seismic energy is dissipated through shear deformation of the link. This is similar to EBFs. The strength and stiffness design of the structure are decoupled, since the section of the replaceable shear link is independent from the spandrel beam. By using replaceable shear links as the dissipative component in SFTS-RSLs, there is a lesser requirement for the development of flexural hinges at beam-ends. In SFTS-RSLs, the damage mainly occurs at the replaceable shear link. Other components remain elastic during seismic loads. Considering the high lateral stiffness of SFTSs, there will be low residual drift after seismic loads. Thus, replacing damaged shear links can achieve the goal of seismic rehabilitation for SFTS-RSLs and reduce the cost of a post-earthquake retrofit.

Currently, Dolatshahi et al. proposed new hybrid energy dissipating steel MRF systems with shear fuses. This combination allows MRFs to use reduced beam sections. The monotonic and cyclic behavior of this frame with a single span-single story was compared with the conventional MRFs with flexural plastic hinges at reduced beam sections through finite element analysis (Nikoukalam and Dolatshahi 2015). One cyclic loading test for a half-scaled one-span and one-story specimen of this frame was carried out to study its hysteretic behaviors (Mahmoudi *et al*. 2016). Hysteretic behaviors of steel MRFs with a beam span-to-depth ratio lower than four and overall seismic performance of structures during dynamic loads was not investigated. Furthermore, the performance of steel MRFs with shear fuses were not compared with conventional steel MRFs without reduced beam sections.

In this paper, 30-story conventional SFTS and SFTS-RSL buildings were designed. Several sub-structures were selected from each design. Finite element models (FEMs) of these substructures were established by ABAQUS to study their hysteretic behaviors under horizontal cyclic loads. FEMs of each building design were established by SAP2000 for seismic performance comparison using static pushover and dynamic analyses.

2. Design concepts for SFTS-RSLs

In steel MRFs, earthquake energy is dissipated through plastic deformation of flexural hinges at beam-ends. As seen in Fig. 1 (*H* refers to the story height), for the SFTSs, the nominal plastic shear strength of beam section V_{pb} is related to the nominal plastic flexural strength of beam section M_{pb}, calculated by Eq. (1)

$$V_{pb} \leq \frac{2M_{pb}}{L_n} \tag{1}$$

where L_{n} is the clear span of the beam. According to Eq. (1), the shear force demands on a beam are increased by decreasing the span of the beam. Because of the shorter external column distance in SFTSs, the shear force on a beam is higher than that of beam in conventional steel MRFs. Thus, increasing the web thickness or cross section height of a beam can increase its shear capacity. However, this results in an increase in the value of M_{pb}. This, then, results in limited plastic deformation of the flexural plastic hinges at beam-ends. Related capacity demands on other SFTS components create an overdesign for this structural system.

For SFTS-RSLs, placing a replaceable shear link at the mid-span of a beam can provide shear and energy dissipation capacities equivalent to beams in SFTSs without increasing the web thickness or beam depth.

Fig. 2 shows details of SFTS-RSLs, in which the replaceable shear link is connected to adjacent beams using a bolted end-plate. Even though the link cross section is smaller than the beam section, considering the theoretical bending moment caused by lateral loads is zero (refer to Fig. 1), lateral stiffness of STFS-RSLs is not significantly lower than that of STFSs.

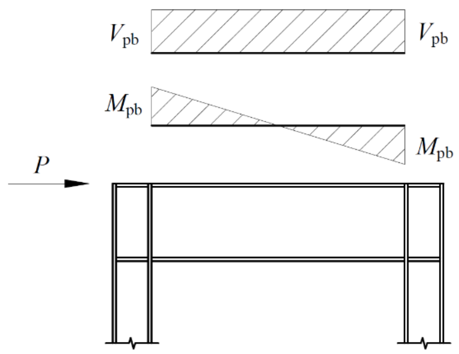

Fig. 1 Shear and moment demands for beam in SFTSs

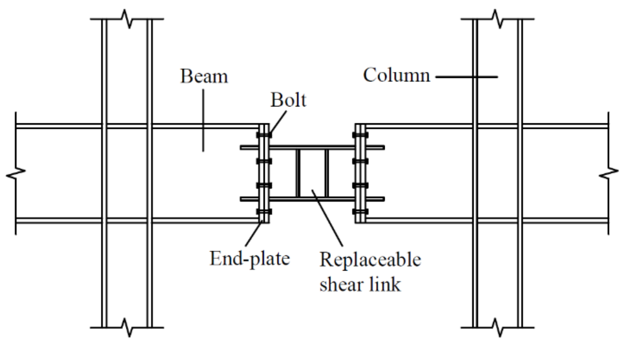

Fig. 2 Concept of SFTS-RSLs

In SFTS-RSLs, when the replaceable shear link yield is dominated by shear force, the design for this shear link is similar to that of the shear link in EBFs. Based on the demands for shear link in EBFs, the length e of the replaceable shear link is determined as below in AISC 341-10 and GB50011-2010

$$e \leq \frac{1.6M_p}{V_p} \tag{2}$$

where M_p and V_p are the nominal plastic flexural strength and nominal plastic shear strength of the shear link, respectively.

To concentrate plastic deformations in the shear link, lower shear strength can be determined using

$$V_L \leq 1.5\frac{2M_{pb}}{L_n} \tag{3}$$

where 1.5 is the recommended overstrength factor for shear links based on the current studies on the performance of shear links (Okazaki *et al*. 2005, Rossi and Lombardo 2007). The V_L of the shear link can be calculated as below in AISC 341-10 and GB50011-2010

$$V_L = 0.60F_{yL}(d_L - 2t_{fL})t_{wL} \tag{4}$$

where F_{yL}, d_L, t_{fL} and t_{wL} are the yield stress of link web, link depth, link flange thickness and link web thickness, respectively.

In the bolted end-plate connections between the replaceable shear link and beams, the end-plate has the same depth as the beam. In AISC 358-10, there are several bolted end-plate connections for special moment frame and intermediate moment frame systems. Considering that the flange end of the shear link experiences flexural deformation during seismic loads, the bolted unstiffened end-plate connection with extended end-plate can be used for the design of link-to-beam connections in SFTS-RSLs. Moreover, the end-plate in link-to-beam connections should have enough strength and stiffness, so that the connections are in elastic with no out-of-plane end-plate deformation when the shear link yields.

3. Designs of SFTSs and SFTS-RSLs

One 30-story conventional SFTS building and one 30-story SFTS-RSL building were designed based on the design codes of GB50010-2010, JGJ99-2015, AISC 341-10 and AISC 358-10. In each design, all structural members used Q345 steel with nominal yield strength of 345 MPa. The building site for each was characterized by PGA of 0.2 g with a 10% exceedance probability in a 50-year period and moderately firm ground conditions.

Fig. 3 shows the two buildings. Shear links were placed in the mid-span of beams in the third and seventh bays in x- and y-directions of the SFTS-RSL building. It because that there is shear lag effect in SFTSs, which results in higher shear force at beam in the beam-to-corner bay and its adjoining bay. Considering the shear links had lower strength capacities than those of the beams, the shear links were placed in the third and seventh bays in the designed SFTS-RSL building, so that they could not increase the shear lag effect and decrease the lateral stiffness of structure. Each building used 3.3 m story heights and nine bays in both x-direction and y-direction. Spans in each direction were 3.0 m. Shear link lengths in the SFTS-RSL building were 700 mm. Roof and floor dead loads were 4.8 kN/m^2. The floor live load, roof live load and snow load used 2, 0.5 and 0.25 kN/m^2 respectively. Additionally, the buildings used the same beam/column cross sections and RC slabs. The structural component sections of SFTS building and SFTS-RSL building are summarized in Table 1 and Table 2, respectively. Furthermore, in the 30-story SFTS-RSL building, the ratios of $e/(M_p/V_p)$ ranged from 1.02 to 1.12.

4. Hysteretic analyses

4.1 finite element models

Three sub-structures from each building were selected to study their hysteretic behaviors. The selected sub-structures are shown in Fig. 4, where L_n is the clear span, d_b is the beam depth, H is the story height and e is the shear link length. For these selected sub-structures, beam span-to-depth ratios (L_n/d_b) less than five were considered, including 3.0, 3.5 and 4.0. Sub-structures were chosen from the 2nd, 16th and 26th stories of each building as indicated in Fig. 3.

Table 1 Structural component sections in 30-story SFTS building

Story	Beams	External columns	Corner columns	Inner Beams	Inner columns
1-5	H850×350×20×30	H500×400×20×25	Box900×900×40	H700×300×25×30	Box800×800×40
6-10	H820×300×20×30	H480×380×20×25	Box850×850×40	H700×300×25×30	Box750×750×35
11-15	H800×300×20×30	H470×360×20×25	Box800×800×40	H700×300×25×30	Box700×700×35
16-20	H750×300×20×25	H450×350×20×25	Box750×750×35	H700×300×25×30	Box650×650×30
21-25	H720×300×20×25	H420×320×20×25	Box700×700×35	H700×300×25×30	Box600×600×30
26-30	H650×300×20×25	H400×300×20×25	Box650×650×30	H700×300×25×30	Box550×550×30

“H” refers to the welded H-shaped section, the following numbers are the section depth (h), flange width (b_f), web thickness (t_w) and flange thickness (t_f), with unit of mm.

Table 2 Structural component sections in 30-story SFTS-RSL building

Story	Shear links	Beams	External columns	Corner columns	Inner Beams	Inner columns
1	H450×250×16×20	H850×350×20×30 (Story 1-5)	H500×400×20×25 (Story 1-5)	Box900×900×40 (Story 1-5)	H700×300×25×30 (Story 1-5)	Box800×800×40 (Story 1-5)
2	H440×250×16×20					
3	H430×250×16×20					
4	H420×250×16×20					
5	H410×250×16×20					
6	H430×250×15×20	H820×300×20×30 (Story 6-10)	H480×380×20×25 (Story 6-10)	Box850×850×40 (Story 6-10)	H700×300×25×30 (Story 6-10)	Box750×750×35 (Story 6-10)
7	H420×250×15×20					
8	H420×220×15×22					
9	H410×220×15×22					
10	H400×220×15×22					
11	H390×220×15×22	H800×300×20×30 (Story 11-15)	H470×360×20×25 (Story 11-15)	Box800×800×40 (Story 11-15)	H700×300×25×30 (Story 11-15)	Box700×700×35 (Story 11-15)
12	H380×220×15×22					
13	H410×200×14×22					
14	H400×200×14×22					
15	H390×200×14×22					
16	H380×200×14×22	H750×300×20×25 (Story 16-20)	H450×350×20×25 (Story 16-20)	Box750×750×35 (Story 16-20)	H700×300×25×30 (Story 16-20)	Box650×650×30 (Story 16-20)
17	H370×200×14×22					
18	H400×200×12×20					
19	H390×200×12×20					
20	H380×200×12×20					
21	H370×200×12×20	H720×300×20×25 (Story 21-25)	H420×320×20×25 (Story 21-25)	Box700×700×35 (Story 21-25)	H700×300×25×30 (Story 21-25)	Box600×600×30 (Story 21-25)
22	H360×200×12×20					
23	H350×200×12×20					
24	H390×200×10×16					
25	H370×200×10×16					
26	H330×200×10×16	H650×300×20×25 (Story 26-30)	H400×300×20×25 (Story 26-30)	Box650×650×30 (Story 26-30)	H700×300×25×30 (Story 26-30)	Box550×550×30 (Story 26-30)
27	H320×200×10×16					
28	H340×200×8×14					
29	H330×200×8×14					
30	H320×200×8×14					

The designations of the finite element models (FEMs) of the above selected sub-structures are summarized in Table 3. These FEMs were established by ABAQUS. In these FEMs, 3D solid elements were used for all the structural components meshed by using the software's "Structure" mesh type. Moreover, the finite element sizes in shear links and bolts were 20 and 5 mm, respectively. The finite element sizes in columns, beams and end-plates were 40 mm. Fig. 5 shows the FEMs and the meshing densities. In the boundary conditions for the FEMs, the out-plane translational DOFs of the beams and columns were constrained and hinge joints were considered for the bottoms of the columns. The multi-linear kinematic hardening rule with the von Mises yielding criterion form of the stress-strain relationship was used as the stress-strain response for the steel in the ABAQUS FEMs, which is shown in Fig. 6, where ε_y and ε_u are the yield and ultimate strains, respectively, σ_y and σ_u are the yield and ultimate stresses, respectively. Nominal yield strength (f_y = 345 MPa for Q345 steel) was adopted for steel materials in these FEMs, including the steel in shear links, columns, beams, end-plates and stiffeners. The nominal yield stress and ultimate stress for the bolts in the FEMs were 640 MPa and 800 MPa, respectively. Furthermore, in the three FEMs, the geometries of the end-plates and stiffeners are shown in Table 4. The elastic modulus E and Poisson's ratio ν are assumed to be 206,000 MPa and 0.3, respectively. The tangent modulus E_t equals to 0.01E based on the properties of Q345 steel. The influence of initial imperfections and residual stress is not considered and P-delta effects were included in the nonlinear analyses.

Two identical displacement-controlled loadings are applied at the top of the columns. The loading history for the nonlinear analyses is shown in Fig. 7, in which Δ and Δ_y are horizontal displacement and yield displacement, respectively. The FEMs were analyzed under a displacement control for one cycle with a magnitude of ±0.25Δ_y, ±0.50Δ_y, ±0.75Δ_y before yielding and three cycles

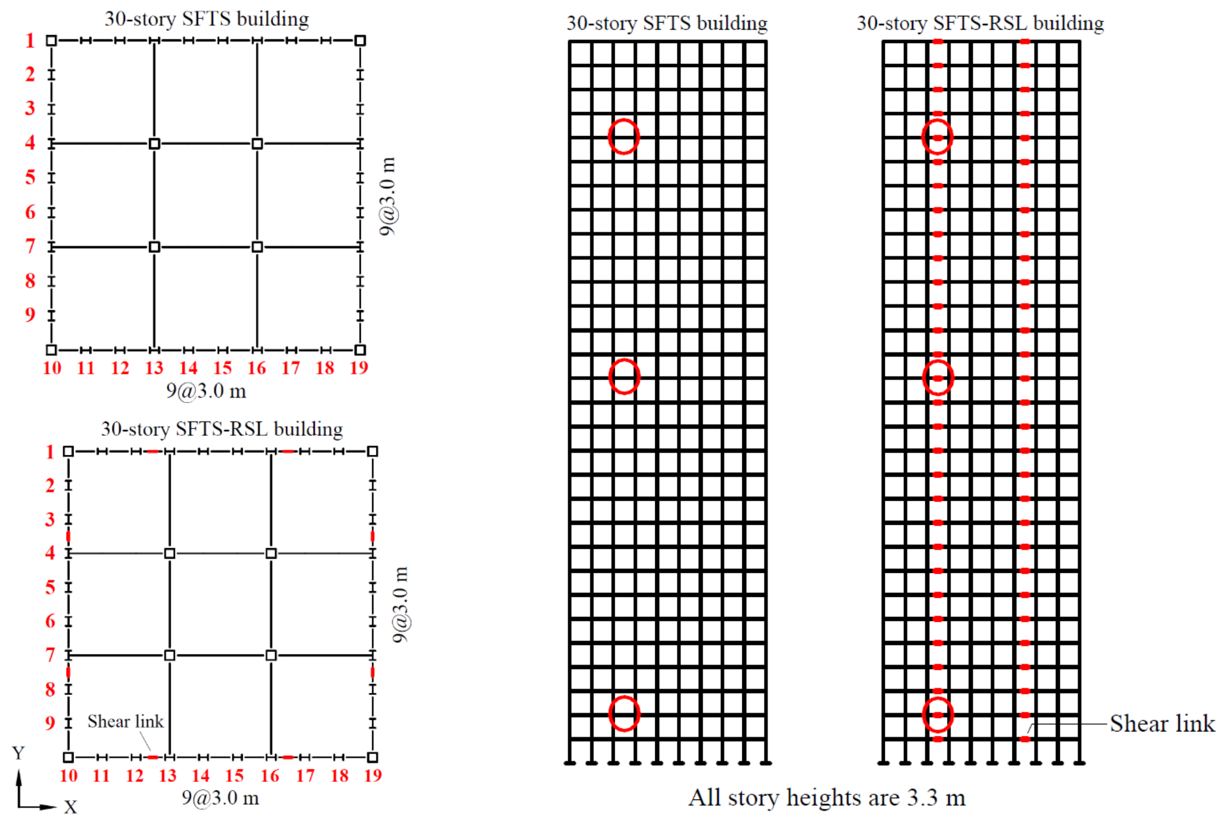

Fig. 3 Building plan and elevation views

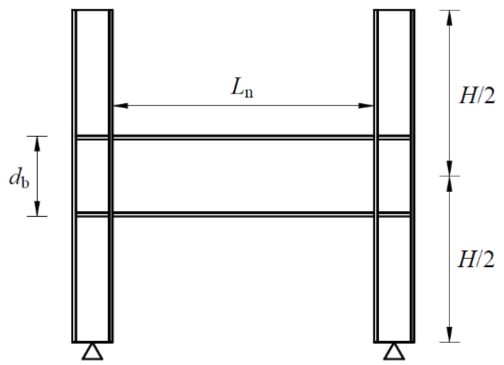

(a) SFTS

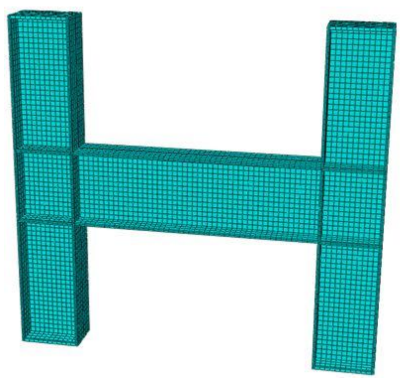

(a) FEM of SFTS sub-structure

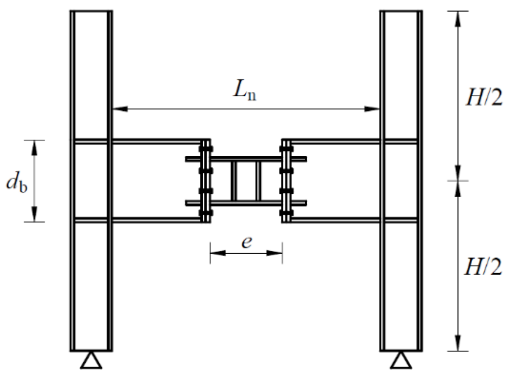

(b) SFTS-RSL

Fig. 4 Selected sub-structures

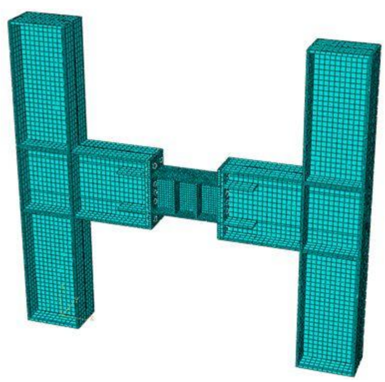

(b) FEM of SFTS-RSL sub-structure

Fig. 5 FEMs and meshing densities

Table 3 Designations of the FEMs

Sub-structures	Designation		
	2nd story	16th story	26th story
SFTS building	SFTS-1	SFTS-2	SFTS-3
SFTS-RSL building	SFTS-RSL-1	SFTS-RSL-2	SFTS-RSL-3

Table 4 Geometries of end-plates and stiffeners

FEMs	SFTS-RSL-1	SFTS-RSL-2	SFTS-RSL-3
End-plates section (height×width×thickness)	850×350 ×50	750×300 ×50	650×300 ×50
Beam-to-column connection stiffener section (height×width×thickness)	450×190 ×30	400×165 ×25	350×140 ×25
Link stiffener section (height×width×thickness)	400×117 ×20	336×93 ×22	298×95 ×16
Link stiffener spacing	2@233	2@233	2@233

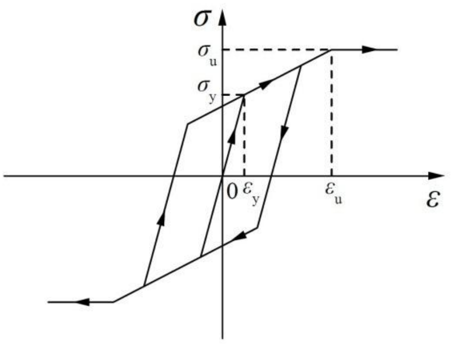

Fig. 6 Stress-strain relations

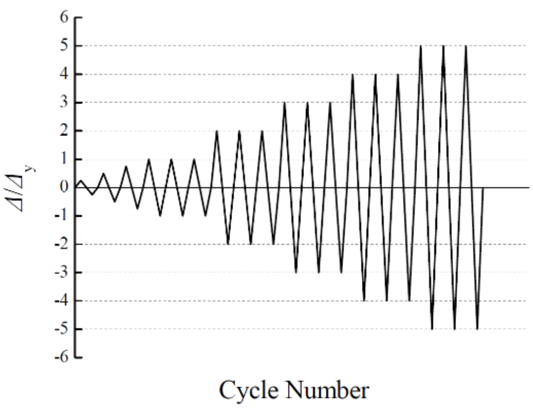

Fig. 7 Loading history for the FEM analyses

(a) Test specimen

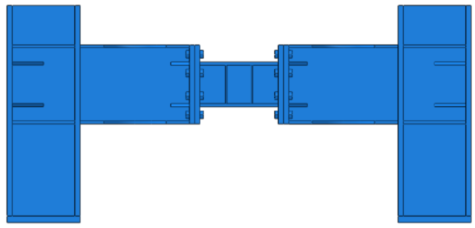

(b) FEM of test spceimen

Fig. 8 FEM of the test specimen

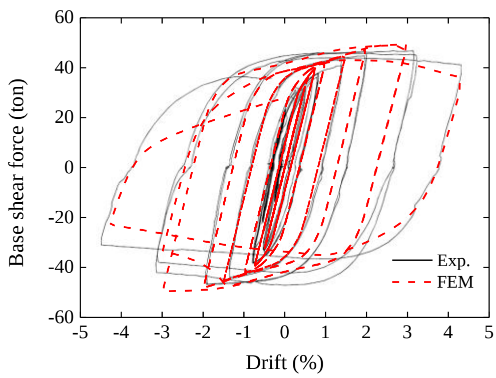

(a) Hysteretic curves

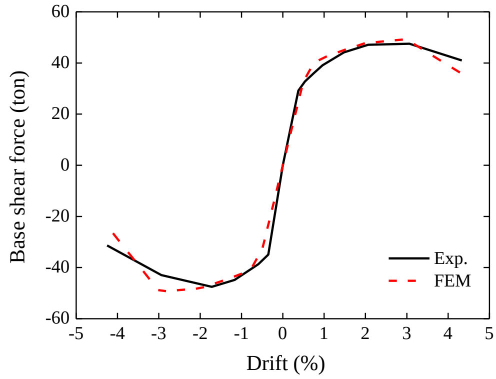

(b) Skeleton curves

Fig. 9 Load-drift curves comparisons

with a magnitude of $\pm\Delta_y$, $\pm2\Delta_y$, $\pm3\Delta_y$, $\pm4\Delta_y$,... $\pm4\Delta_{target}$ after yielding. The displacement corresponding to the 5% story drift was considered as the target displacement Δ_{target} (Ellingwood 2001) for all FEMs in the nonlinear numerical analyses.

4.2 Model verification

One cyclic loading test for a half-scaled one-span and one-story specimen of the steel MRF with RBS connections and replaceable shear link was carried out by Mahmoudi (Mahmoudi *et al*. 2016). Based on the measured dimensions of this test specimen, the specimen was modeled using previously discussed assumptions. The FEM analysis results were compared with the test results of the specimen to verify the modeling approach. The FEM of the test

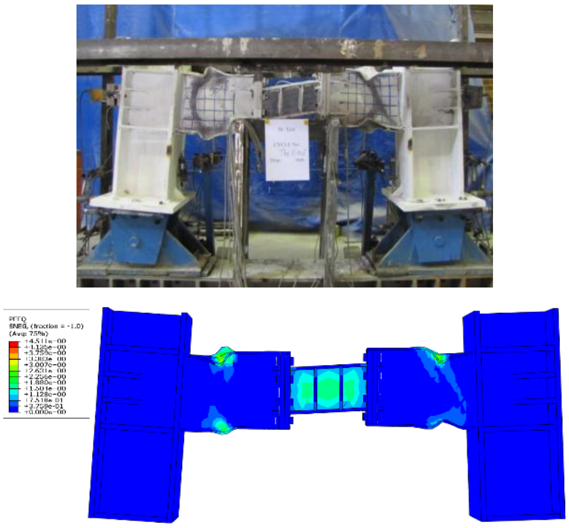

Fig. 10 Deformed geometry comparison

specimen used the 3D solid element in ABAQUS. Fig. 8 shows the test specimen and its FEM. Fig. 9 compares the load-drift curves of the test specimen and the corresponding FEM. It shows that the FEM analysis curves were fully spindle-shaped and in good agreement compared with the test curves. In the FEM hysteretic curves, the negative zone was slightly different from the test curves. This is because when the FEM was loaded at the second cycle of drift of 3%, the FEM had greater buckling at RBS connections than that of test specimen, leading to the more obvious strength degradation of FEM. Fig. 10 shows the deformed geometry comparison of the test specimen and its FEM. The results indicated that the FEM could properly simulate the link web yielding and local buckling in web and flange at the beam-ends that were observed in the test specimen. Therefore, the simulation results are considered to be in good agreement with the experimental results.

4.3 Analysis results

4.3.1 Hysteretic curves

The hysteretic curves of SFTS FEMs and the corresponding SFTS-RSL FEMs during cyclic loads from the nonlinear analyses are shown in Fig. 11. Before reaching 5% story drift, FEMs SFTS-1, SFTS-2 and SFTS-3 undergone obvious strength degradation due to local buckling occurring at the beam web, near the plastic hinge zone, and the column flange near the beam-to-column connection. They reached a maximum at 4% story drift. The SFTS-RSL FEMs reached 5% story drift, producing stable and expanding hysteretic loops, with no deterioration in stiffness and strength. The hysteretic loops for each of the

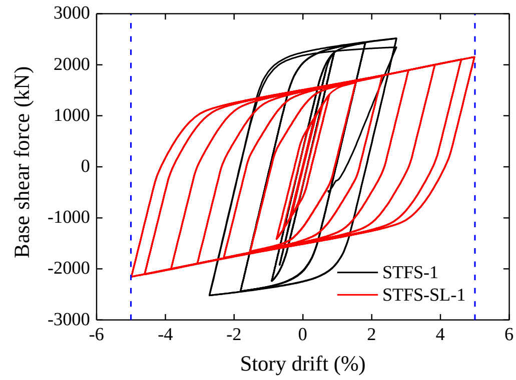

(a) SFTS-1 and SFTS-SL-1

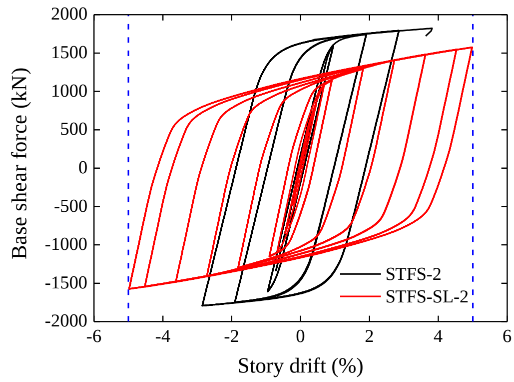

(b) SFTS-2 and SFTS-SL-2

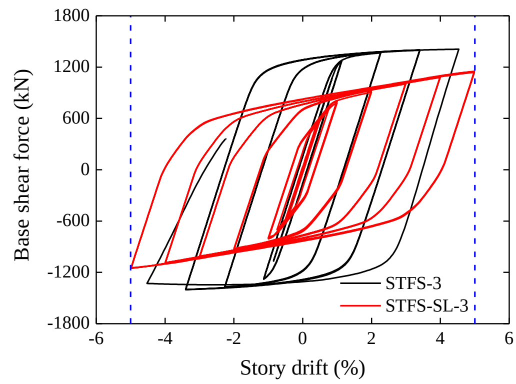

(c) SFTS-3 and SFTS-SL-3

Fig. 11 Hysteretic curves

SFTS-RSL FEM were quite broad, indicating significant energy dissipation capacity.

4.3.2 Stiffness and load-bearing capacity

Table 5 indicates the initial elastic stiffness K_e for all FEMs. Note that FEM had similar K_e values for both positive and negative directions. K_e values are lower for

Table 5 Elastic stiffness of HPGFEMs

Load directions	Elastic stiffness (kN/mm)	SFTS FEMs			SFTS-RSL FEMs		
		SFTS-1	SFTS-2	SFTS-3	SFTS-RSL-1	SFTS-RSL-2	SFTS-RSL-3
Positive	K_e	86.4	56.8	38.4	82.0	54.2	37.0
Negative	K_e	86.4	56.8	38.4	82.0	54.2	37.0

Table 6 Load-bearing capacities of FEMs

Load directions	Base shear force (kN)	SFTS FEMs			SFTS-RSL FEMs		
		SFTS-1	SFTS-2	SFTS-3	SFTS-RSL-1	SFTS-RSL-2	SFTS-RSL-3
Positive	P_y	1921.4	1333.7	1065.1	1215.4	1068.6	700.5
	P_{max}	2519.2	1821.7	1409.3	2151.8	1574.3	1150.6
	P_{max}/P_y	1.31	1.37	1.32	1.77	1.47	1.64
Negative	P_y	1923.6	1335.5	1066.9	1215.8	1078.4	702.1
	P_{max}	2520.2	1793.0	1400.9	2154.9	1575.2	1151.1
	P_{max}/P_y	1.31	1.34	1.31	1.77	1.46	1.64

Table 7 Ductility of FEMs

Load directions	Drift (%)	SFTS FEMs			SFTS-RSL FEMs		
		SFTS-1	SFTS-2	SFTS-3	SFTS-RSL-1	SFTS-RSL-2	SFTS-RSL-3
Positive	θ_y	0.9	1.0	1.1	0.8	0.9	1.0
	θ_{max}	2.7	3.8	4.5	5.0	5.0	5.0
	μ	3.00	3.80	4.09	6.25	5.56	5.01
Negative	θ_y	0.9	1.0	1.1	0.8	0.9	1.0
	θ_{max}	2.7	2.9	4.5	5.0	5.0	5.0
	μ	3.00	2.99	4.09	6.25	5.56	5.01

SFTS-RSL relative to SFTS in all FEMs. This indicates that using a shear link at beam mid-span does not result in significant lower initial elastic stiffness for the STFS-RSL system. Thus, placing a shear link at the beam mid-span where the flexural demand due to the lateral load is theoretically zero had almost no impact on the initial lateral stiffness of the frame.

Table 6 presents the load-bearing capacities of the FEMs. These include yield strength P_y and maximum strength P_{max}. The P_y of each FEM was almost same in both positive and negative directions. The P_y of SFTS-RSL-1 was 36.7% lower than that of SFTS-1. For SFTS-RSL-2 and SFTS-RSL-3, relative to SFTS-2 and SFTS-3, the differences were 19.9% and 34.2%, respectively. This P_y reduction occurs because the shear link has lower shear capacity than that of the deep spandrel beam. This results in a lower P_y of SFTS-RSL relative to SFTS. However, when the FEMs became damaged or reached the target drift, the P_{max} of SFTS-RSL-1 was 14.6% lower than that of SFTS-1. For SFTS-RSL-2 and SFTS-RSL-3 compared with SFTS-2 and SFTS-3, the differences are 12.2% and 17.8%, respectively. This indicates that the P_{max} of a SFTS-RSL FEM was not significantly lower than that of the corresponding SFTS FEM. Furthermore, the P_{max}/P_y ratios of SFTS FEMs range from 1.31 to 1.37. SFTS-RSL FEM ratios range from 1.46 to 1.77. The SFTS-RSLs exhibit more stable hardening behavior compared to the corresponding SFTS frames.

4.3.3 Ductility capacity

The ductility coefficient μ was used to judge the ductility of the FEMs and is defined as $\mu = \theta_{max}/\theta_y$, where θ_y and θ_{max} are the yield and maximum story drift, respectively. Table 7 lists the θ_y, θ_{max} and μ of the FEMs, respectively. The μ of SFTS-RSL FEMs were higher than those of the corresponding SFTS FEMs. The μ of SFTS-RSL-1 was 2.1 times higher than that of SFTS-1. For SFTS-RSL-3 compared with SFTS-3, the difference was 1.2 times. The μ of SFTS-RSL-2 were 1.5 and 1.9 times higher than that of SFTS-2 at positive and negative directions, respectively. Note that the SFTS-RSL has a better ductility relative to the corresponding SFTS.

4.3.4 Energy dissipation capacity

Fig. 12 displays energy dissipation performance for each FEM based on the hysteretic curves. While dissipation values for each SFTS model are similar, they are out performed in every case by their SFTS-RSL counterpart. The dissipated energy of SFTS-RSL-1 was 3.4 times higher than that of SFTS-1. For SFTS-RSL-2 and SFTS-RSL-3 compared with SFTS-2 and SFTS-3, the differences are 2.4 times and 1.4 times, respectively. It because that the SFTS-

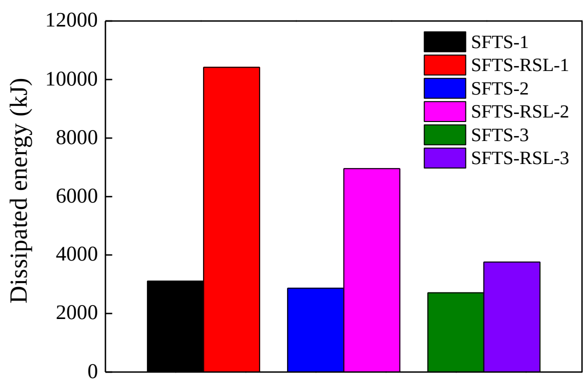

Fig. 12 Energy dissipation

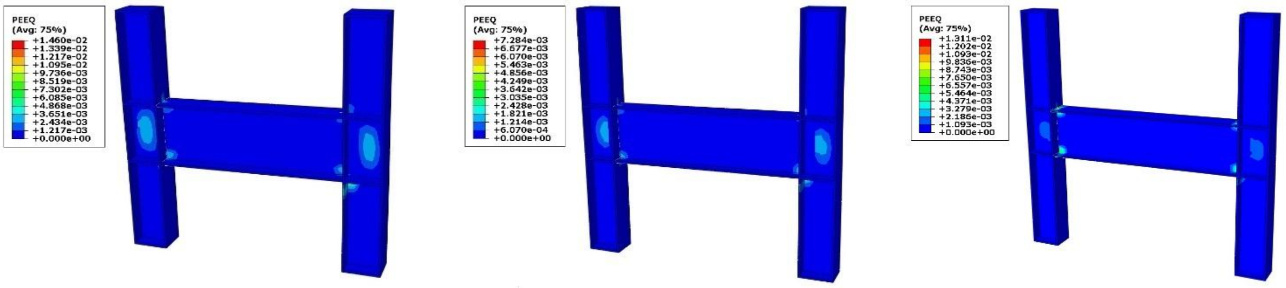

SFTS-1 SFTS-2 SFTS-3

(a) Yield state

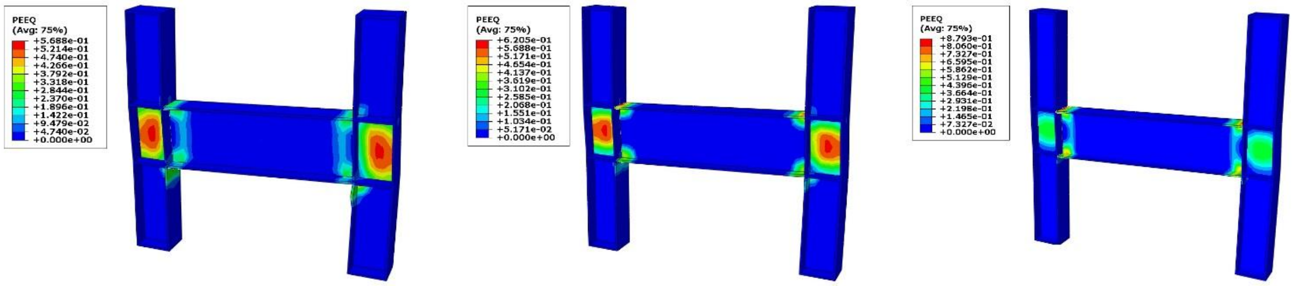

SFTS-1 SFTS-2 SFTS-3

(b) Ultimate state

Fig. 13 Distributions of PEEQ in SFTS FEMs

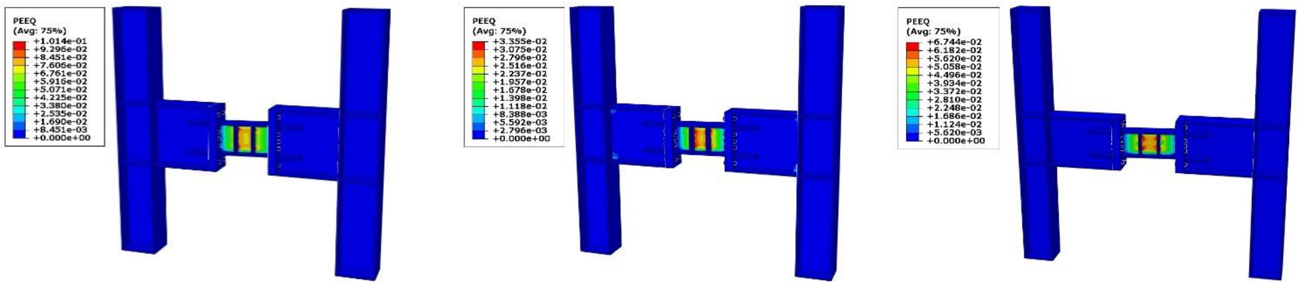

SFTS-RSL-1 SFTS- RSL-2 SFTS- RSL-3

(a) Yield state

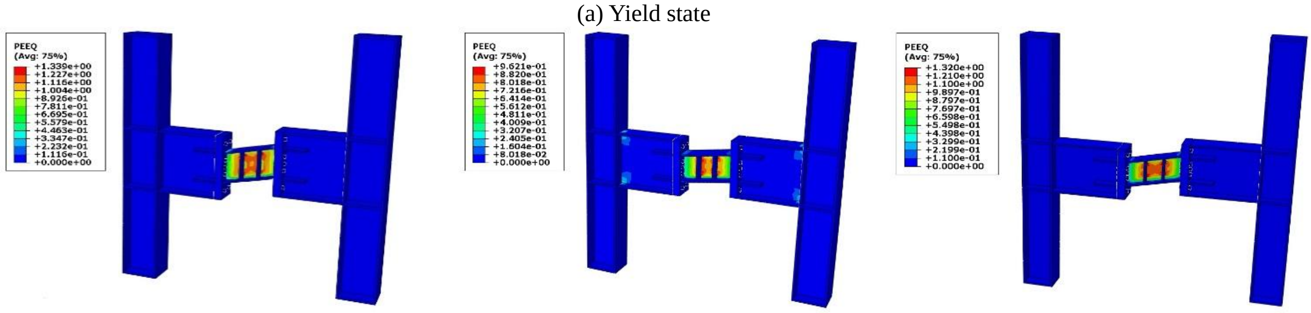

SFTS- RSL-1 SFTS- RSL-2 SFTS- RSL-3

(b) Ultimate state

Fig. 14 Distributions of PEEQ in SFTS-RSL FEMs

RSL had a better ductility compared with the corresponding SFTS. Thus, based on the analysis results, the SFTS-RSL had a significant better energy dissipation capacity than that of the corresponding SFTS.

4.3.5 Failure mechanism

Figs. 13 and 14 present the deformations and the distributions of plastic equivalent strain (PEEQ) for SFTS and SFTS-RSL FEMs, respectively. In the SFTS, yield zones occurred at beam-ends, column-ends and the beam-to-column connections. In the ultimate state, plastic strains developed in the beam-ends were significantly lower than those in the beam-to-column connection zones. By increasing the L_n/d_b ratios, strain values within these zones decreased. Local buckling occurred in the flange of column-ends in the SFTS-1 and SFTS-2. This was not observed in

SFTS-3. Comparing the SFTS FEMs, it can be concluded that at beam span-to-depth ratios lower than five, significant yield occurs in column-ends and beam-to-column connection zones. This may increase the possibility of collapse. The lower span-to-depth ratio limits the development of plastic hinges at the beam-ends in SFTS, resulting in lower energy dissipation capacity of the beam and higher plastic strains in beam-to-column connection zones.

When SFTS-RSL FEMs yielded, plastic strains were developed throughout the entire depth of the shear links. The beams, columns and beam-to-column connection zones were in elastic in SFTS-RSL-1 and SFTS-RSL-3. Only slight plastic strain occurred at the beam-ends in SFTS-RSL-2. When the SFTS-RSL FEMs were in the ultimate state, the plastic strains within the shear link web obviously increased while no plasticity took place at the other structural components. Plastic strain increased slightly at beam-ends in SFTS-RSL-2. In addition, plastic strain was concentrated in the shear link web with relatively little appearing in the shear link flanges. The shear link design performed as expected. It could achieve the goal of seismic rehabilitation for SFTS-RSLs by replacing the damage shear links with the new ones.

5. Static and dynamic analyses

5.1 Finite element models

The FEMs of the designed 30-story SFTS and 30-story SFTS-RSL buildings were established by SAP2000. In the two FEMs, the plastic hinges were defined at column-ends and beam-ends using the plastic hinges for steel column and beam in SAP2000 software based on the model presented in Tables 5-6 of FEMA-356 for steel column and beam. For the shear link, the model presented in Tables 5-6 of FEMA-356 was considered for the nonlinear behavior, as seen in Fig. 15. The ultimate shear force of the shear link V_u = $1.4V_p$ according to experimental results of shear links (Okazaki and Engelhardt 2015). Moreover, the immediate occupancy deformation Δ_{IO}, life safety plastic deformationΔ_{LS} and collapse prevention deformation Δ_{CP} of the shear link were conducted using the parameters as suggested by Tables 5-6 of FEMA-356.

Table 8 Fundamental natural periods

Designs	Period (s)		
	T_1	T_2	T_3
30-story SFTS buildings	3.85	3.85	2.49
30-story SFTS-RSL buildings	3.86	3.86	2.50
Period difference [a]	0.26%	0.26%	0.40%

[a] refers to ($T_{SFTS\text{-}RSL}$-T_{SFTS})/ T_{SFTS}, where $T_{SFTS\text{-}RSL}$ and T_{SFTS} are the period of SFTS-RSL and SFTS, respectively

Table 8 shows the fundamental natural periods of the two buildings. The difference in period between the two designs was lower than 0.5%. This indicates almost no impact on lateral stiffness by placing the shear link at the beam mid-span with the flexural demand due to lateral loads being theoretically zero.

The FEMs of the analytical 30-story SFTS and SFTS-RSL buildings were established by SAP2000. The designations of the two FEMs were SFTS and SFTS-RSL, respectively. In developing the FEMs, beam elements were used for all structural members. Nominal yield strength was adopted for the steel. The elastic modulus and Poisson's ratio are assumed to be 206,000 MPa and 0.3, respectively. The influence of initial imperfections and residual stress is not considered and *P*-delta effects were included in the analyses. Nonlinear hinges were defined at the links, beams and columns. Moreover, the analysis was conducted using life safety structural performance level as well as the nonlinear behavior of shear link by FEMA-356. For shear link, the model presented in Tables 5-6 of FEMA-356 was considered for nonlinear behaviors. The ultimate shear force of the shear link V_u = $1.4V_p$ according to experimental results of shear links (Okazaki and Engelhardt 2015).

5.2 Static analyses and results

The higher-mode displacement-controlled pattern in FEMA 274 was selected for the static pushover analyses. These analyses were performed along the x-direction of the

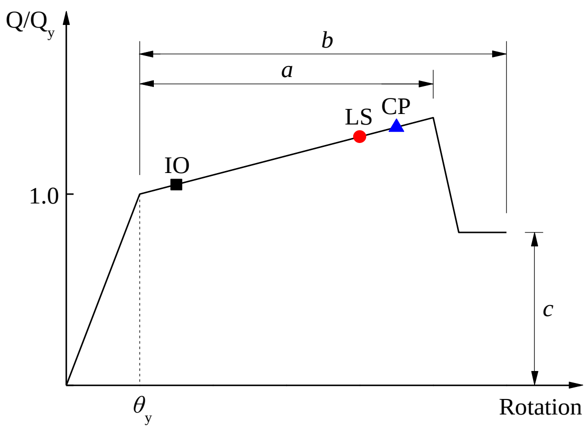

Fig. 15 Generalized force-deformation relation for shear link (FEMA-356)

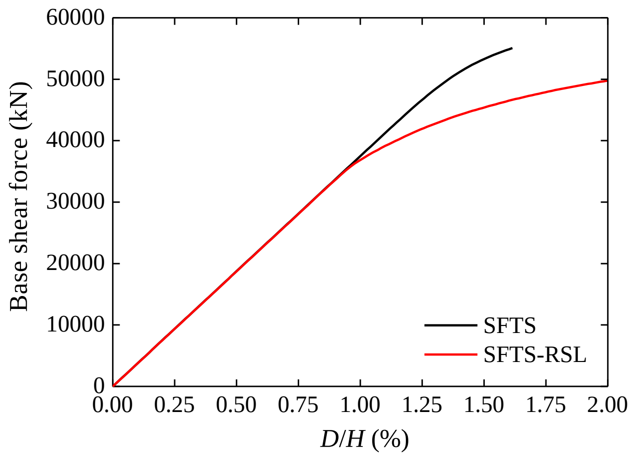

Fig. 16 Base shear force-roof drift curves

Table 9 Load-bearing capacity and ductility

FEMs	SFTS	SFTS-RSL
K_e (kN/mm)	40.0	39.9
P_y (kN)	47378.6	33923.6
P_{max} (kN)	55073.0	49782.1
θ_y (%)	1.3	0.9
θ_{max} (%)	1.6	2.0
P_{max}/P_y	1.2	1.5
$\mu = \theta_{max} / \theta_y$	1.2	2.2

structure in Fig. 3. In the pushover analyses, D/H = 2% was selected as the target displacement, where D and H are the roof displacement and total height of structure. The lateral resistant capacity of SFTS and SFTS-RSL were investigated through the nonlinear pushover analyses.

Fig. 16 shows the results of the static pushover analyses for FEMs SFTS and SFTS-RSL. The curves show that the maximum roof drift of SFTS-RSL reached the target drift of 2%, but the maximum roof drift of SFTS was just higher than 1.5%. However, the load-bearing capacity of SFTS was greater than that of SFTS-RSL when they reached the same roof drift. Table 9 lists the initial lateral stiffness K_e, the yield strength P_y, the maximum load-bearing capacity P_{max}, yield roof drift θ_y and the maximum roof drift θ_{max} of SFTS and SFTS-RSL. The K_e of SFTS and SFTS-RSL were nearly same, which indicated that placing the shear link at the beam mid-span almost had no effects to the initial elastic lateral stiffness of the structure. The P_y of SFTS was much higher than that of SFTS-RSL, but the P_{max} of SFTS-RSL was just 9% lower than that of SFTS. The P_{max}/P_y was 1.5 for SFTS-RSL, which was higher than that of 1.2 for SFTS. It indicated that the SFTS-RSL had a more stable hardening behavior compared with the SFTS. In addition, the ductility coefficient μ of SFTS-RSL was nearly two times higher than that of SFTS, which indicated that the ductility of SFTS-RSL was much better.

Fig. 17 shows the plastic hinge distributions of SFTS and SFTS-RSL at the yield and ultimate states, respectively. When reaching the yield state, the distribution of plastic hinges distribution of SFTS was nonuniform for the SFTS. Most plastic hinges were observed on some beam-ends in the middle stories. In the yield state, the SFTS-RSL had a uniform distribution of plastic hinges at shear link. When reaching the ultimate state, all shear links were in inelastic and the plastic hinges observed at shear links and beam-ends. The plastic hinges were mostly distributed at beam-ends and some in the column-ends on some stories in the SFTS when it reached the ultimate state. Furthermore, the developments of plastic hinges in SFTS were lower than that in SFTS-RSL.

5.3 Dynamic analyses and results

5.3.1 Ground motions

FEMs were subjected to nonlinear dynamic analyses with various ground motions to study and compare relative performance. The dynamic analyses were performed using a set of ground motions and the ground motions were selected based on their properties on spectrum characteristics, accelerations and durations. The earthquakes were loaded along the x-direction of the structure in Fig. 3. The

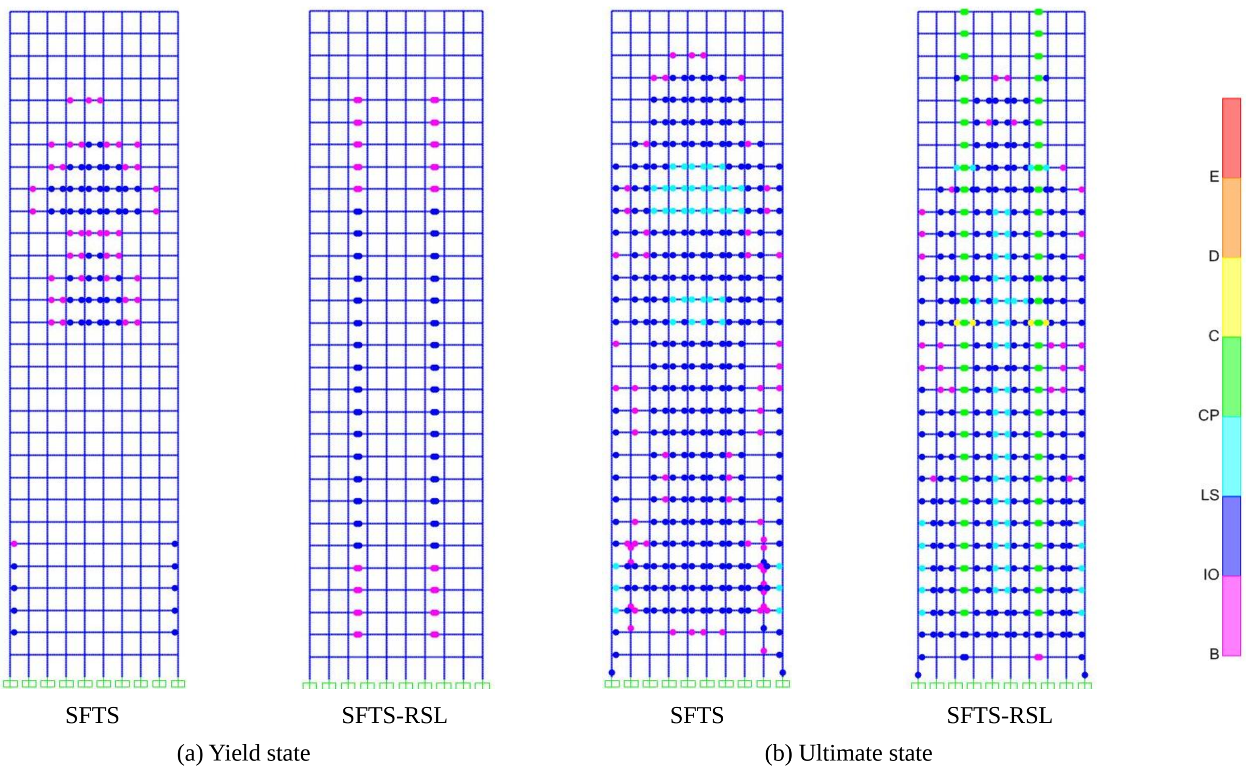

Fig. 17 Plastic hinges distributions

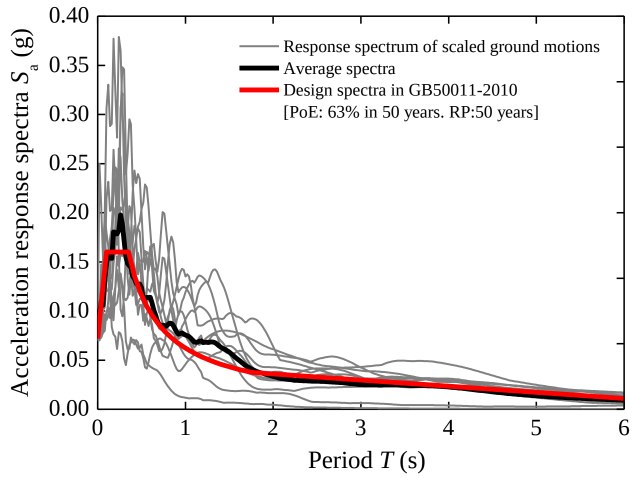

Fig. 18 Design spectra and scaled earthquake spectra

seismological properties of the ground motions are summarized in Table 10. Three levels of seismic hazard were employed: 50%, 10% and 2% probability of exceedance in a 50-year period. These earthquakes were defined as frequent, moderate and severe earthquakes. Moreover, in JGJ99-2015, the corresponding PGAs for frequent, moderate and severe earthquakes are 0.07, 0.2 and 0.4 g, respectively. The scale factors in Table 9 are defined to scale the PGAs of the selected ground motions to the corresponding PGAs of the three level earthquakes. The acceleration response spectra of the ensemble of accelerograms, along with the design acceleration spectrum are shown in Fig. 18.

5.3.2 Dynamic analysis results

Fig. 19 compares maximum interstory drifts during ground motions for SFTS and SFTS-RSL. Interstory drifts increased as with earthquake intensity. Based on

Table 10 Characteristics of ground motions

Earthquakes	Year	Station	Record	Pr. of exc. (% in 50 yrs)	Magnitude	Source distance (km)	*PGA* (g)	*PGV* (cm/s)	Scale factors
Imperial Valley	1979	Delta	IMPVALL/H-DLT352	50/10/2	6.53	12.45	0.24	26.0	0.29/0.83/1.67
Loma Prieta	1989	CDMG 47381 Gilroy Array #3	LOMAP/G03000	50/10/2	6.93	12.82	0.56	35.6	0.13/0.36/0.71
Cape Mendocino	1992	Rio Dell Overpass	CAPEMEND/RIO360	50/10/2	7.01	14.33	0.39	44.1	0.18/0.51/1.03
Chi-Chi, Taiwan	1999	TCU095	ChiChi/TCU095-W	50/10/2	7.6	43.4	0.379	62	0.29/0.79/1.35
Landers	1992	Yermo Fire Station	LANDERS/YER360	50/10/2	7.28	23.62	0.24	51.4	0.29/0.83/1.67
Kern County	1952	Taft Lincoln School	KERN/TAF021	50/10/2	7.4	41	0.156	15.3	0.71/1.92/3.27
Kobe, Japan	1995	Shin-Osaka	KOBE/SHI090	50/10/2	6.9	19.15	0.24	37.8	0.29/0.83/1.67
Northridge	1994	Castaic-Old Ridge Route	NORTHR/ORR090	50/10/2	6.7	20.1	0.568	52.1	0.19/0.53/0.90
Duzce, Turkey	1999	Bolu	DUZCE/BOL090	50/10/2	7.14	12.04	0.73	56.4	0.10/0.27/0.55
Superstitn Hills	1987	El Centro Imp. Co. Cent	SUPERST/B-SUP135	50/10/2	6.5	5.6	0.894	42.2	0.12/0.34/0.57

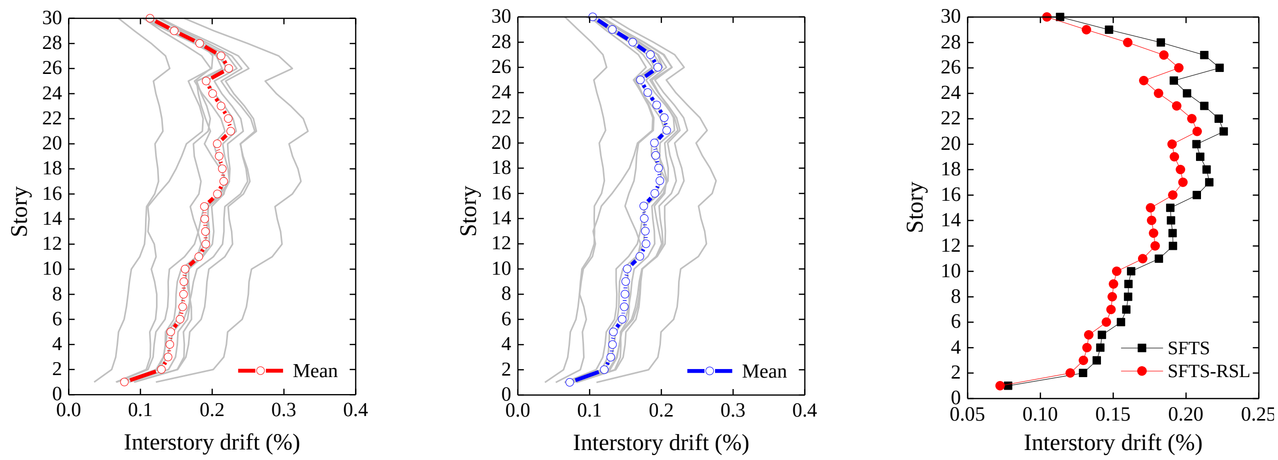

(a) Frequent earthquakes

Fig. 19 Interstory drifts comparison for SFTS and SFTS-RSL a comparison of mean curves, the SFTS-RSL design outperformed its SFTS counterpart across all categories. The relative differences are 12.2%, 12.6% and 13.1%. Moreover, as seen in Figs. 19(b) and (c), the mean maximum interstory drifts of SFTS and SFTS-RSL were much lower than the interstory drift limitation of 2% during

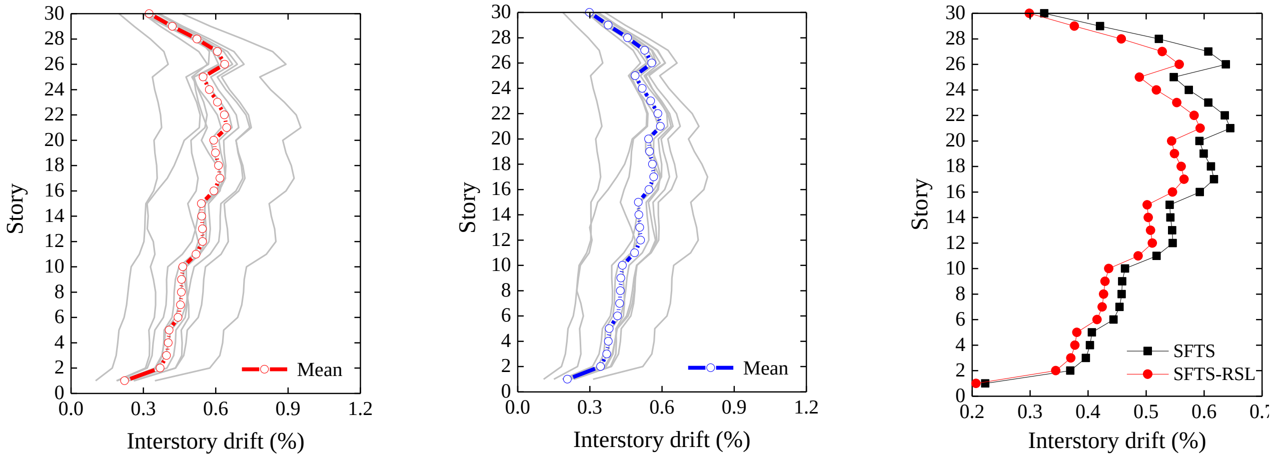

SFTS SFTS-RSL Interstory drift comparison

(b) Moderate earthquakes

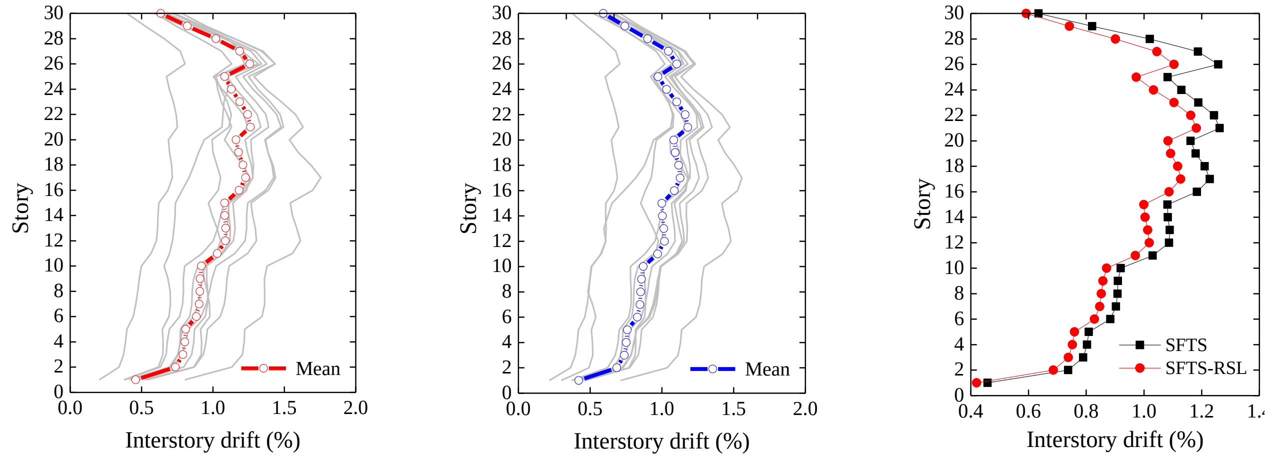

SFTS SFTS-RSL Interstory drift comparison

(c) Severe earthquakes

Fig. 19 Continued

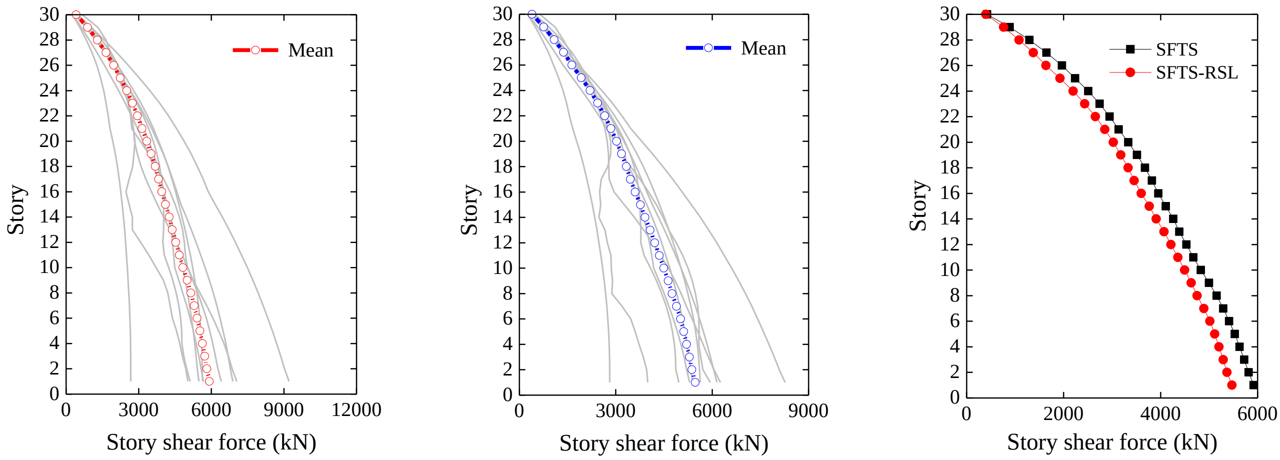

SFTS SFTS-RSL Story shear force comparison

(a) Frequent earthquakes

Fig. 20 Story shear force comparison of SFTS and SFTS-RSL

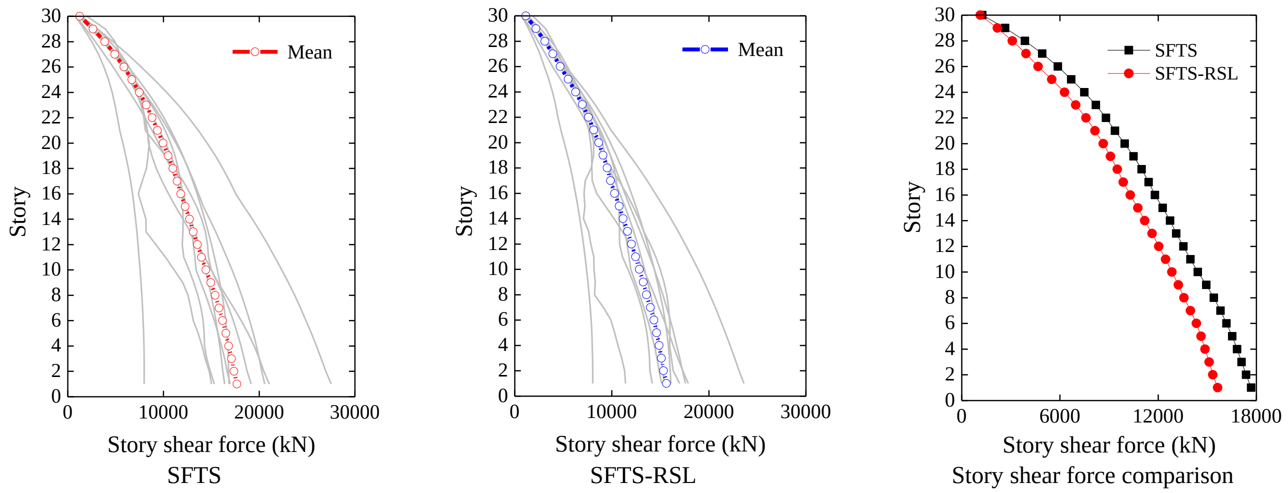

(b) Moderate earthquakes

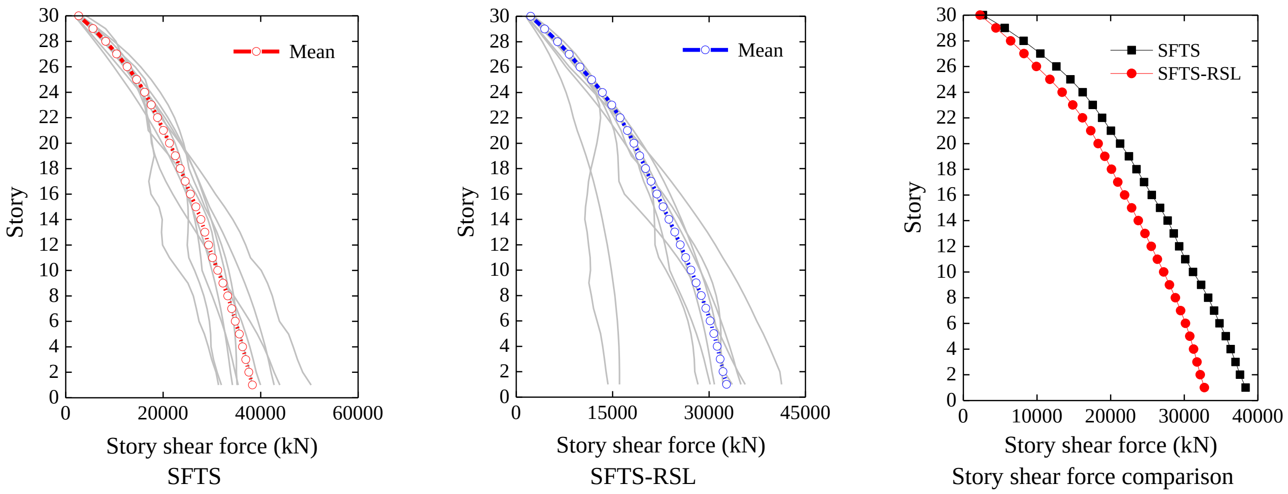

(c) Severe earthquakes

Fig. 20 Continued

the moderate and severe earthquakes. This comparison reveals that across categories the SFTS-RSL exhibited lower interstory drifts. Placing a shear link at the beam mid-span reduced interstory drifts of the frame during various earthquake loads.

Fig. 20 compares the story shear force for SFTS and SFTS-RSL under the three previously categorized earthquake loads. During the frequent, moderate and severe earthquakes, the mean maximum story shear forces of SFTS-RSL were lower than those of the SFTS by 16.8%, 20.5% and 21.6% respectively. Table 11 lists the categorical mean maximum base shear force $P_{\max,m}$ of SFTS and SFTS-RSL during the earthquakes with different intensities. The $P_{\max,m}$ of SFTS-RSL was lower than that of the SFTS from 7.6% to 14.6%, earthquake intensity. These results suggest that the SFTS-RSL could help reduce earthquake damage to the structure.

Fig. 21 shows a comparison of column axial forces on the SFTS and SFTS-RSL during earthquakes and the column number was identified in Fig. 3. Columns in the 1st, 6th, 11th, 16th, 21st and 26th stories were considered. Axial forces on columns one through ten in the flange frame

Table 11 Mean maximum base shear force comparison of SFTS and SFTS-RSL

FEMs	Mean maximum base shear force $P_{\max,m}$ (kN)		
	Frequent earthquakes	Moderate earthquakes	Severe earthquakes
SFTS	5919.3	17680.8	38331.7
SFTS-RSL	5471.4	15632.5	32742.5
Base shear force difference [a]	7.6%	11.6%	14.6%

[a] refers to $(P_{\text{SFTS-RSL}}-P_{\text{SFTS}})/P_{\text{SFTS}}$, where $P_{\text{SFTS-RSL}}$ and P_{SFTS} are the base shear force of SFTS-RSL and SFTS, respectively.

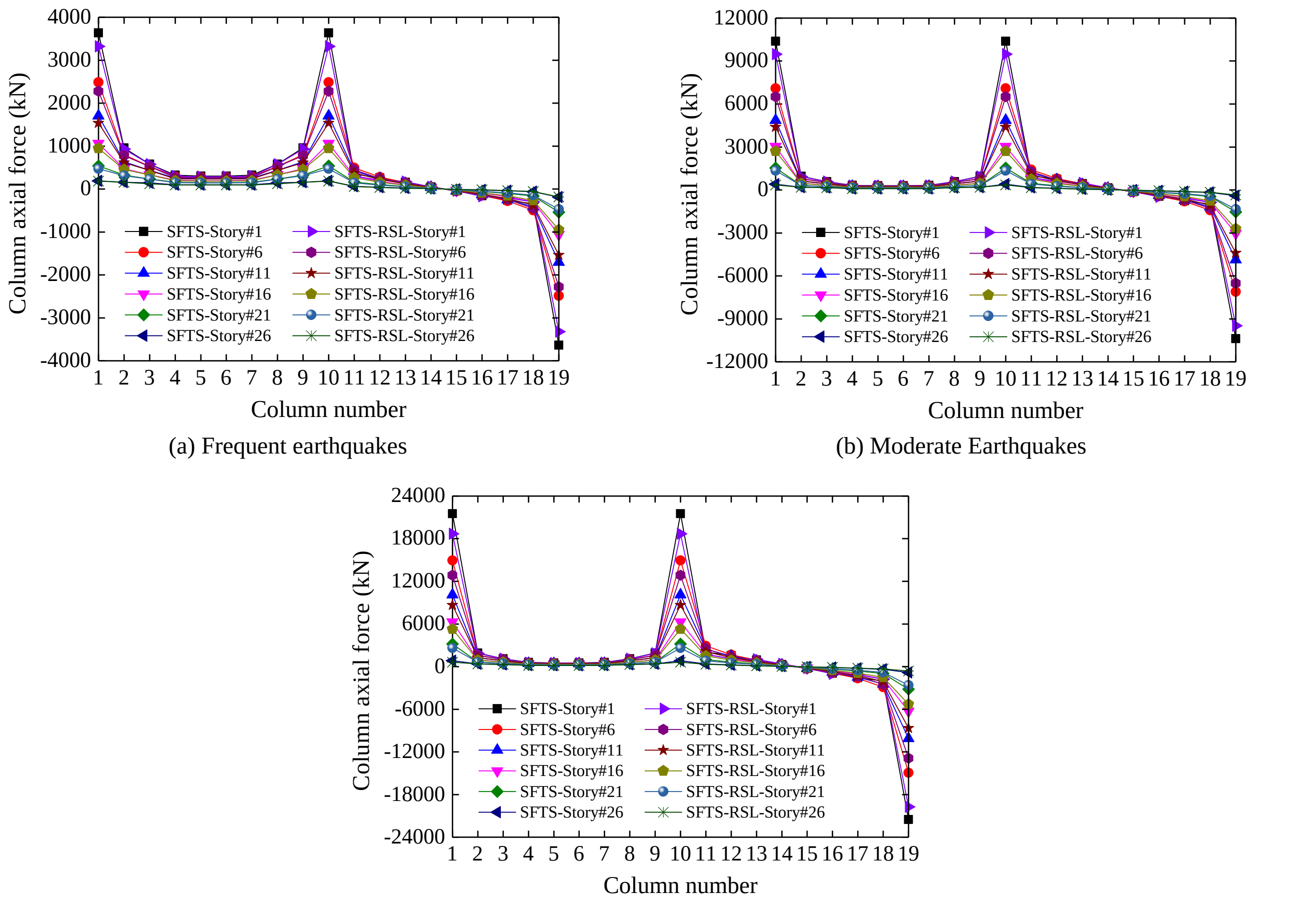

(a) Frequent earthquakes

(b) Moderate Earthquakes

(c) Severe earthquakes

Fig. 21 Columns axial force comparison of SFTS and SFTS-RSL

(y-direction, refer to Fig. 3) were nearly the same for each FEM during the earthquakes with different intensities. In the web frame (x-direction, refer to Fig. 3), the column axial forces in the upper stories of SFTS-RSL were slightly lower than those of the SFTS. In the lower stories, SFTS-RSL results were significantly lower. These differences ranged from 0.8% to 21.6% during frequent earthquakes and from 2.9% to 21.7% and 6.2% to 27.7% during moderate and severe earthquakes, respectively.

The results indicate that placing a shear link at the beam mid-span did not increase the shear lag effects on the steel framed-tube structure. However, STFS-RSL had lower column axial forces compared with SFTS.

Fig. 22 shows the mean residual interstory drifts of SFTS-RSL during moderate and severe earthquake ground motion. These values are well below the 0.5% limit suggested in research by McCormick *et al.* (2008) as a threshold beyond which it becomes more economical to rebuild rather than repair a structure. The SFTS-RSL shows residual story drifts less than 0.05% and 0.2% during moderate and severe earthquakes, respectively. Moreover, the residual link rotation angle of SFTS-RSL corresponding to residual interstory drift of 0.5% is 0.02 rad, and the maximum residual link rotation angle of SFTS-RSL was 0.002 and 0.007 rad for moderate and severe earthquake ground motions, respectively. This points to the expectation that shear link replacement could be an effective repair

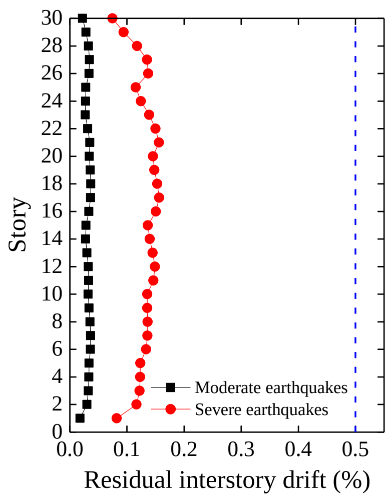

Fig. 22 Residual interstory drifts of SFTS-RSL during earthquakes

strategy after an earthquake.

Fig. 23 shows plastic hinge distributions for SFTS and SFTS-RSL during severe earthquakes (Kobe and Chi-Chi ground motions). There were more plastic hinges in the SFTS, most were observed at beam-ends and some were at column-ends in the lower stories. Many plastic hinges at the beam-ends approached the state of CP (collapse prevention).

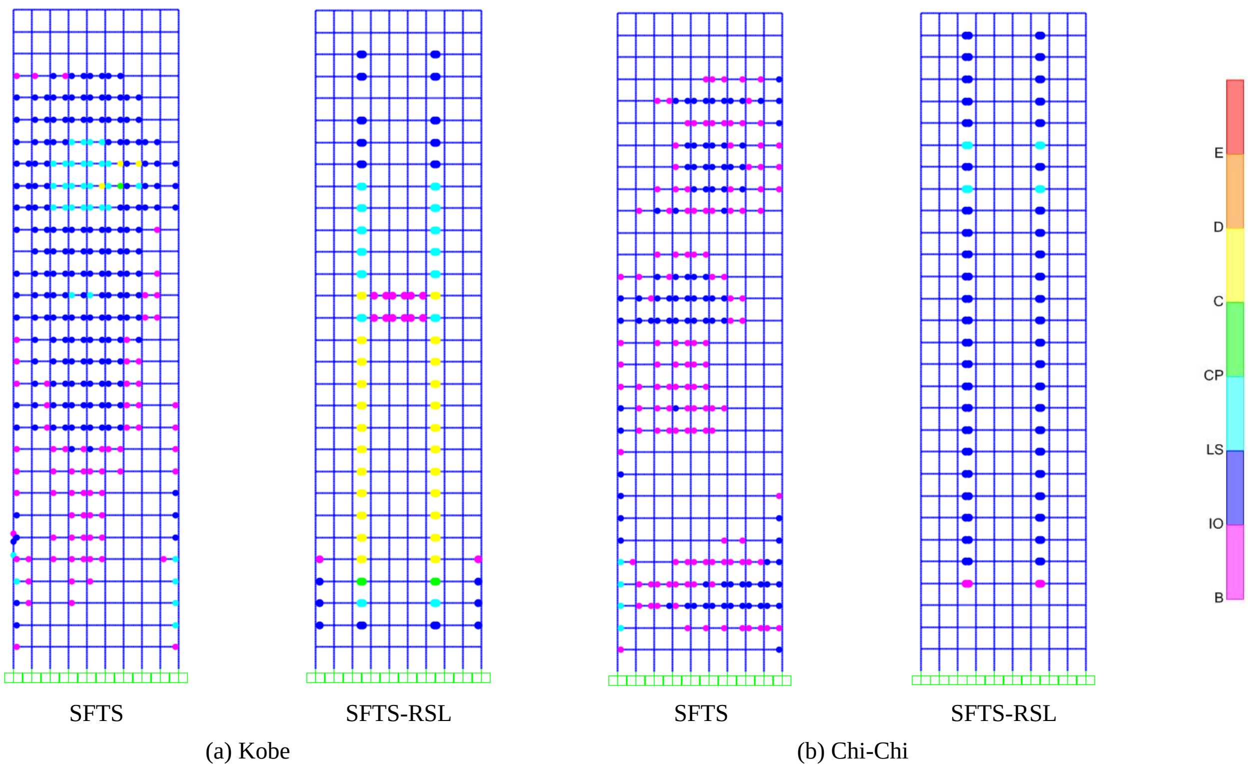

Fig. 23 Plastic hinge distributions during severe earthquakes

In such cases, beam repair may be difficult.

In the SFTS-RSL, most plastic hinges were observed at the shear links. Only some were at beam-ends. The development of plastic hinges at the shear links was much higher than at the beam-ends where these components just reached the yield state. The indication is that earthquake energy is dissipated primarily through shear link deformation. Most other structural components were still in elastic. This also suggests that the SFTS-RSL is a reliable dual resistant system. Thus, replacing damaged shear links can help achieve the goal of seismic rehabilitation for SFTS-RSL structures.

6. Advantages and applicability of SFTS-RSL

Based on cyclic, static pushover and dynamic analyses, both SFTS-RSL and SFTS have similar initial lateral stiffness. Placing a shear link at the beam mid-span does not increase shear lag effects on the structure. Compared with SFTS, SFTS-RSL had lower yield and maximum strengths, which is a weakness of SFTS-RSL. It is noteworthy that the SFTS-RSL has better ductility and energy dissipation capacity. The proposed system had lower interstory drifts, base shear force and story shear force under earthquake conditions. In SFTS-RSL, the plasticity concentrated on the shear link while the other structural components were in elastic and the residual story drifts were lower than 0.2% during the seismic loads. Thus, compared with SFTS, the SFTS-RSL is a reliable dual resistant system with better ductility and energy dissipation capacities. It enables structural repair through replacement of damaged shear links after earthquakes.

Using a replaceable shear link at the beam mid-span in SFTS has a slight effect on its elastic lateral stiffness. This technique offers improvements in ductility and energy dissipation for SFTS with span-to-depth ratios of 3.0 and 3.5. This advantage diminishes as span-to-depth ratios increase beyond 4.0. This occurs because the plastic deformation capacities of beam-ends improve with higher beam span-to-depth ratios. Thus, the purposed methodology that placing a shear link at the beam mid-span can obviously improve the ductility and energy dissipation capacities of SFTS with the beam span-to-depth ratios lower than 4.0 is effective based on the analysis results set out in this paper.

7. Conclusions

Considering the characteristic of deep spandrel beams with low span-to-depth ratios in SFTS, replaceable shear links can be proposed as the ductile fuse at the mid length of the deep beam to improve seismic performance. In SFTS-RSL, the seismic energy is dissipated through the shear deformation of the link. 30-story SFTS and SFTS-RSL buildings were designed. Several SFTS and SFTS-RSL sub-structures were selected from the each design to study their hysteretic behaviors. Static and nonlinear dynamic analyses were carried out to investigate the seismic performance of the each building. The following conclusions can be drawn within the limitations of the research:

- SFTS-RSL and SFTS had similar initial lateral stiffness and shear lag effects, indicating that placing a shear link at the beam mid-span where the flexural demand due to the lateral load is theoretically zero had almost no effect on the initial lateral stiffness and did not increase shear lag effects.

- Compared with SFTS, SFTS-RSL had lower yield and maximum strengths but more stable hardening behaviors. RSL-SFTS had better ductility and energy dissipation capacities. During earthquake loads, RSL-SFTS had lower interstory drifts, base shear force and story shear force than those of SFTS.
- In RSL-SFTS, the plasticity concentrated on the shear link while the other structural components were in elastic and the residual story drifts were lower than 0.2% during the seismic loads. SFTS-RSL is a reliable dual resistant system and provides an opportunity to repair the structure by replacing damaged shear links after earthquakes.
- The proposed methodology of placing a shear link at the beam mid-span can obviously improve the ductility and energy dissipation capacities of SFTS with the beam span-to-depth ratios lower than 4.0 is effective, based on the analysis results set out in this paper.

Acknowledgments

The authors are grateful for the partial financial support from the National Natural Science Foundation of China (Grant No. 51708444) and Shaanxi Natural Science Foundation (Grant No. 2018JQ5074). Thanks go to Mike Brewes from Nipissing University, Canada for his assistance in proofreading this article.

References

AISC 341-10 (2010), Seismic provisions for structural steel buildings; Chicago, IL, USA.

AISC 358-10 (2010), Prequalified connections for special and intermediate steel moment frames for seismic applications; Chicago, IL, USA.

Alavi, A., Rahgozar, P. and Rahgozar, R. (2018), "Minimum-weight design of high-rise structures subjected to flexural vibration at a desired natural frequency", *Struct. Des. Tall Special Build.*, **27**(15), e1515.

Bahrami, S., Madhkhan, M., Shirmohammadi, F. and Nazemi, N. (2017), "Behavior of two new moment resisting precast beam to column connections subjected to lateral loading", *Eng. Struct.*, **132**, 808-821.

Caprili, S., Mussini, N. and Salvatore, W. (2018), "Experimental and numerical assessment of EBF structures with shear links", *Steel Compos. Struct., Int. J.*, **28**(2), 123-138.

Charney, F.A. and Pathak, R. (2008a), "Sources of elastic deformation in steel frame and framed-tube structures: part 1: simplified subassemblage models", *J. Constr. Steel Res.*, **64**(1), 87-100.

Charney, F.A. and Pathak, R. (2008b), "Sources of elastic deformations in steel frame and framed-tube structures: part 2: detailed subassemblage models", *J. Constr. Steel Res.*, **64**(1), 101-117.

Ellingwood, B.R. (2001), "Earthquake risk assessment of building structures", *Reliabil. Eng. Syst. Safety*, **74**(3), 251-262.

FEMA (1997), NEHRP commentary on the guidelines for the seismic rehabilitation of buildings; FEMA-274, Federal Emergency Management Agency (FEMA); Washington D.C., USA.

FEMA (2000), State of the art report on connection performance; FEMA-355D, Federal Emergency Management Agency (FEMA); Washington D.C., USA.

GB50011-2010 (2010), Code for seismic design of buildings; Beijing, China.

Ramirez, C.M., Lignos, D.G., Miranda, E. and Kolios, D. (2012), "Fragility functions for pre-northridge welded steel moment-resisting beam-to-column connections", *Eng. Struct.*, **45**(2284), 574-584.

Sheet, I.S., Gunasekaran, U. and Macrae, G.A. (2013), "Experimental investigation of cft column to steel beam connections under cyclic loading", *J. Constr. Steel Res.*, **86**(86), 167-182.

Memari, M., Mahmoud, H. and Ellingwood, B. (2014), "Post-earthquake fire performance of moment resisting frames with reduced beam section connections", *J. Constr. Steel Res.*, **103**, 215-229.

JGJ 99-2015 (2015), Technical specification for steel structure of tall buildings; Beijing, China.

Kamgar, R. and Rahgozar, R. (2013), "A simple approximate method for free vibration analysis of framed tube structures", *Struct. Des. Tall Special Buildi.*, **22**(2), 217-234.

Lian, M., Su, M.Z. and Guo, Y. (2015), "Seismic performance of eccentrically braced frames with high strength steel combination", *Steel Compos. Struct., Int. J.*, **18**(6), 1517-1539.

Lian, M., Su, M.Z. and Guo, Y. (2017), "Experimental performance of Y-shaped eccentrically braced frames fabricated with high strength steel", *Steel Compos. Struct., Int. J.*, **24**(4), 441-453.

Mahmoudi, F., Dolatshahi, K.M., Mahsuli, M., Shahmohammadi, A. and Nikoukalam, M.T. (2016), "Experimental evaluation of steel moment resisting frames with a nonlinear shear fuse", In: *Geotechnical and Structural Engineering Congress*.

Malekinejad, M., Rahgozar, R., Malekinejad, A. and Rahgozar, P. (2016), "A continuous-discrete approach for evaluation of natural frequencies and mode shapes of high-rise buildings", *Int. J. Adv. Struct. Eng.*, **8**(3), 269-280.

McCormick, D., Aburano, H., Ikenaga, M. and Nakashima, M. (2008), "Permissible residual deformation level for building structures considering both safety and human elements", *Proceedings of the 14th World Conference on Earthquake Engineering*, Beijing, China.

Moon, K.S. (2010), "Stiffness-based design methodology for steel braced tube structures: a sustainable approach", *Steel Constr.*, **32**(10), 3163-3170.

Nikoukalam, M.T. and Dolatshahi, K.M. (2015), "Development of structural shear fuse in moment resisting frames", *J. Constr. Steel Res.*, **114**, 349-361.

Oh, K., Lee, K., Chen, L., Hong, S.B. and Yang, Y. (2015), "Seismic performance evaluation of weak axis column-tree moment connections with reduced beam section", *J. Constr. Steel Res.*, **105**, 28-38.

Okazaki, T. and Engelhardt, M.D. (2015), "Cyclic loading behavior of EBF links constructed of ASTM A992 steel", *J. Constr. Steel Res.*, **63**(6), 751-765.

Okazaki, T., Arce, G., Ryu, H.C. and Engelhardt, M.D. (2005), "Experimental study of local buckling, overstrength, and fracture of links in eccentrically braced frames", *J. Struct. Eng.*, **131**(10), 1526-1535.

Rahgozar, R., Ahmadi, A.R., Ghelichi, M., Goudarzi, Y., Malekinejad, M. and Rahgozar, P. (2014), "Parametric stress distribution and displacement functions for tall buildings under lateral loads", *Struct. Des. Tall Special Build.*, **23**(1), 22-41.

Rossi, P.P. and Lombardo, A. (2007), "Influence of the link overstrength factor on the seismic behaviour of eccentrically braced frames", *J. Constr. Steel Res.*, **63**(11), 1529-1545.
Shayanfar, M.A., Barkhordari, M.A. and Rezaeian, A.R. (2012), "Experimental study of cyclic behavior of composite vertical shear link in eccentrically braced frames", *Steel Compos. Struct., Int. J.*, **12**(1), 13-29.
Taranath, B.S. (2011), *Structural Analysis and Design of Tall Buildings: Steel and Composite Construction*, CRC Press.
Tavakoli, R., Rahgozar, R. and Kamgar, R. (2018), "The best location of belt truss system in tall buildings using multiple criteria subjected to blast loading", *Civil Eng. J.*, **4**(6), 1338-1353.

CC